

Rapid mapping of compound eye visual sampling parameters with FACETS, a highly automated wide-field goniometer

John K. Douglass¹ · Martin F. Wehling¹

Received: 11 May 2016 / Revised: 27 July 2016 / Accepted: 29 July 2016 / Published online: 21 September 2016
© Springer-Verlag Berlin Heidelberg 2016

Abstract A highly automated goniometer instrument (called FACETS) has been developed to facilitate rapid mapping of compound eye parameters for investigating regional visual field specializations. The instrument demonstrates the feasibility of analyzing the complete field of view of an insect eye in a fraction of the time required if using non-motorized, non-computerized methods. Faster eye mapping makes it practical for the first time to employ sample sizes appropriate for testing hypotheses about the visual significance of interspecific differences in regional specializations. Example maps of facet sizes are presented from four dipteran insects representing the Asilidae, Calliphoridae, and Stratiomyidae. These maps provide the first quantitative documentation of the frontal enlarged-facet zones (EFZs) that typify asilid eyes, which, together with the EFZs in male Calliphoridae, are likely to be correlated with high-spatial-resolution acute zones. The presence of EFZs contrasts sharply with the almost homogeneous distribution of facet sizes in the stratiomyid. Moreover, the shapes of EFZs differ among species, suggesting functional specializations that may reflect differences in visual ecology. Surveys of this nature can help identify species that should be targeted for additional studies, which will elucidate fundamental principles and constraints that govern visual field specializations and their evolution.

Keywords Acute zones · Bright zones · Insect vision · Visual field specializations · Spatial sampling arrays

Introduction

Many animals possess regional eye specializations that enhance aspects of the visual information within particular portions of the visual field (Land 1997; Land and Nilsson 2002). In particular, arthropod compound eyes have been demonstrated to have an astonishing variety of eye designs (Land 1981, 1989), which often include regional specializations that appear to be correlated with visual requirements. Much has been learned by examining such specializations in a few dozen species, yet when considered in light of the tremendous diversity of highly visual arthropods, our current insights into the functional significance and diversity of visual field specializations must still be considered rather preliminary. To develop a broader and deeper understanding of how regional specializations are related to visual ecology, it is important to develop methods that will allow more rapid assessments of visual field topographies in large numbers of species. This study describes a goniometer instrument called FACETS (Fast Apparatus for Compound Eye Topography Studies) that has been designed with this goal in mind. We use it here to map facet diameters.

Compound eyes are composed of from hundreds to thousands of individual ommatidia, the anatomical and functional units that underlie each cuticular facet on the surface of the eye (see Land 1989; Land and Nilsson 2002; Cronin et al. 2014). Each ommatidium samples the visual information from a limited 3-D acceptance angle (typically 1°–3° in insects), so that the overall angular extent of the eye's visual field is determined by the number of ommatidia and the orientations of the individual ommatidial axes.

Various regional specializations within the field of view can locally enhance attributes of visual information such as spatial resolution and light capture, or may confer polarization sensitivity or control spectral sensitivity (reviews:

✉ John K. Douglass
john.douglass.3.ctr@us.af.mil

¹ Eglin Air Force Base, 101 W. Eglin Blvd., Eglin AFB, FL 32542, USA

Hardie 1986; Stavenga 1992; Land 1997; Land and Nilsson 2002; Cronin et al. 2014). In apposition compound eyes, the most thoroughly studied regional adaptations are those that involve reductions in inter-ommatidial angles ($\Delta\phi$), producing “acute zones” (AZs) with enhanced spatial acuity. Acute zones are often also marked by enlarged facets (e.g., Collett and Land 1975; Horridge and Duelli 1979; Rossel 1979; Land and Eckert 1985; Hardie 1986; Dahmen 1991; Smolka and Hemmi 2009), which are consistent with theoretical predictions of the architecture of acute zones based on optical and anatomical constraints (Warrant et al. 2007). An added benefit of enlarged facets is that light sensitivity to point sources increases in proportion to facet lens area, with important consequences for signal-to-noise ratios, temporal resolution, and contrast sensitivity. Thus, “bright zones” of enlarged facets may occur in the absence of any distinctive acute zone, as in the male blowfly *Chrysomya megacephala* (van Hateren et al. 1989). Alternatively, within the same eye, there may be regions with enlarged facets and reduced interommatidial angles that do not coincide exactly, creating somewhat distinct “acute” and “bright” zones (e.g., Rossel 1979; Straw et al. 2006; Somanathan et al. 2009).

Thus, although many mapping studies of compound eyes have focused on acuity, it is clearly also important to measure facet diameters. The software for the FACETS instrument has been configured first to measure facet sizes, as enlarged facet zones (EFZs) strongly indicate the presence of a regional specialization. They are typically associated with acute zones, and facet sizes are conveniently measured from both living specimens and museum specimens. Compatibility of the instrument with museum specimens is particularly useful for broad comparative studies, which can lead to more detailed investigations of living specimens of selected species.

Elegant techniques are available for evaluating functionally important eye parameters, notably those involving the non-invasive use of pseudopupils and “eye shine” reflections to measure visual acuity, binocular zones, spectral sensitivity, rhabdom organization, and light- and dark-adaptational pigment movements in vivo (e.g., Franceschini and Kirschfeld 1971; Beersma et al. 1975, 1977; Stavenga 1979). Using these techniques, a number of previous studies have provided informative visual acuity maps of selected insects and crustaceans (reviews: Land 1997; Land and Nilsson 2002; Cronin et al. 2014), and based on these studies, general conclusions have been drawn about how animals with compound eyes make use of regional visual specializations.

It is well established that visual predators, as well as males of many species that capture their prey (or mates) in flight, typically possess a specialized frontal or fronto-dorsal acute zone with enlarged facets and reduced

interommatidial angles. However, little is known about the ways in which acute zones differ according to details of predator and prey visual ecology. For example, what design principles and constraints govern the size, shape, and topography of specialized eye regions? Are the acute zones of all insect predators roughly equivalent, or have distinct architectures evolved that may reflect specialized hunting strategies? More generally, to what extent is panoramic vision (e.g., the detail needed for optic flow pattern recognition) traded off against acute zones? These are especially pressing questions for very small visual predators that are severely constrained by having small eyes with relatively few ommatidia (Land 1999; Gonzalez-Bellido et al. 2011). Beyond their basic scientific import, insights into strategies for optimizing localized image enhancements can also lead to improvements in man-made digital imaging devices (e.g., Roberts et al. 2014; Warrant et al. 2014).

To understand the principles and constraints that govern the evolution of visual adaptations, hypotheses should be tested by conducting comparative studies of the complete visual fields in multiple specimens. An ultimate goal would be to analyze not only one or two, but several functionally relevant visual parameters at once. A major challenge for expanding the database of detailed eye maps, however, is that evaluating the full field of view entails making measurements at hundreds of precisely controlled eye orientations. Thus, the process of completely mapping even a single parameter from one eye can be very time-consuming and tedious. It comes as no surprise that with relatively few exceptions (e.g., Beersma et al. 1977; Sherk 1977, 1978a, b; Zeil et al. 1986; Rutowski et al. 2009), individual investigations of this nature have mainly been limited to one or two species. In other cases, a broader comparative scope may be achieved (in part) by restricting measurements to forward-looking eye regions (e.g., Horridge 1978), or using flattened corneal replicas to measure facet diameters (see “Discussion”).

In recent years, mapping studies of compound eyes have taken steps toward automation by employing some combination of computer-controlled motors, digital cameras, and interactive software to assist with image-processing (e.g., Dahmen 1991; Marshall and Land 1993; Petrowitz et al. 2000; Krapp and Gabbiani 2005; Smolka and Hemmi 2009). The FACETS instrument builds upon these advances with a more comprehensive approach. To acquire data more rapidly and minimize the need for human supervision, all repetitious instrument motions have been motorized, and data sampling, image analyses, and data processing are all at least partially automated. In addition, to support investigations of diverse species, the instrument was designed to accommodate a wide range of eye sizes, and to sample the entire field of view of most eyes without needing to remount the specimen.

The instrument is currently used to semi-automatically measure, across a uniform angular distribution of sampling orientations, local facet diameters, and the geometry (square vs. hexagonal packing) of the facet lattice. Since these two parameters can be well measured in either living or non-living subjects, they can be used for broader mapping surveys than would be practical when studying eye characteristics that must be measured in vivo. In the future, in addition to the semi-automated facet size and lattice geometry measurements, further improvements to the FACETS software should make it possible to automate measurements of interommatidial angles.

Materials and methods

Overview of the goniometer instrument

The main components of the instrument are a microscope, a digital camera, a custom-built goniometer, controller units for motorized rotation and translation stages, and a Windows PC with software.

Electronic components and electrical connections

Figure 1 diagrammatically shows the major components of the instrument and the electrical connections. A Windows 7 PC (HP model Z400, Hewlett-Packard, Palo Alto, CA, USA), equipped with three monitors and software written in Matlab 2014b (Mathworks Inc., Natick, MA, USA),

is used to operate the goniometer’s motor controllers and acquire images from a monochrome digital video camera (Grasshopper Express model GX-FW-28S5 M-C, Point Gray Instruments, Richmond BC, Canada, with Point Gray PCIE adapter card). The PC uses serial USB connections to communicate with each of four motor controllers.

Three Micos “Pollux-1” motor controllers (Edmund Optics, Inc.) are used to operate three miniature linear translation stages within the goniometer (x' , y' , and z'), each with a 10-mm travel range (model VT-21-2SM, Micos USA, Irvine, CA). A Newport ESP 301 three-axis motor controller operates two rotary stages that define goniometer axes *A* and *B*, respectively (RS-A, Newport #URS100BCC and RS-B, Newport #SR50-CC), and an additional SR50-CC rotary stage (RS-F) is used to focus the microscope. Some additional details of the microscope are provided in the “Appendix.”

Mechanical and optical components

The overall optomechanical design of the goniometer is shown schematically in Fig. 2a, with photographic views in Fig. 2b, c. The microscope and the goniometer are bolted to an optical breadboard with a 1-inch square grid of mounting holes (#SG 35-4, Newport Instruments, Irvine CA, USA). This grid provides a fixed frame of reference for aligning all components of the instrument, including a mirror (described below) that is used to align one of the rotary axes. To prevent building vibrations from affecting instrument alignment or degrading image quality, the breadboard

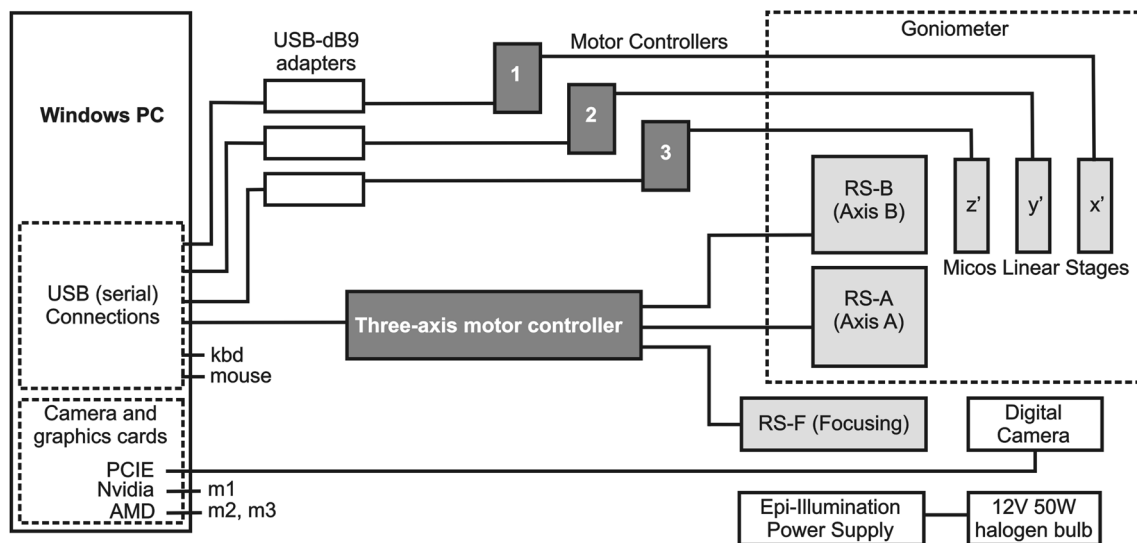
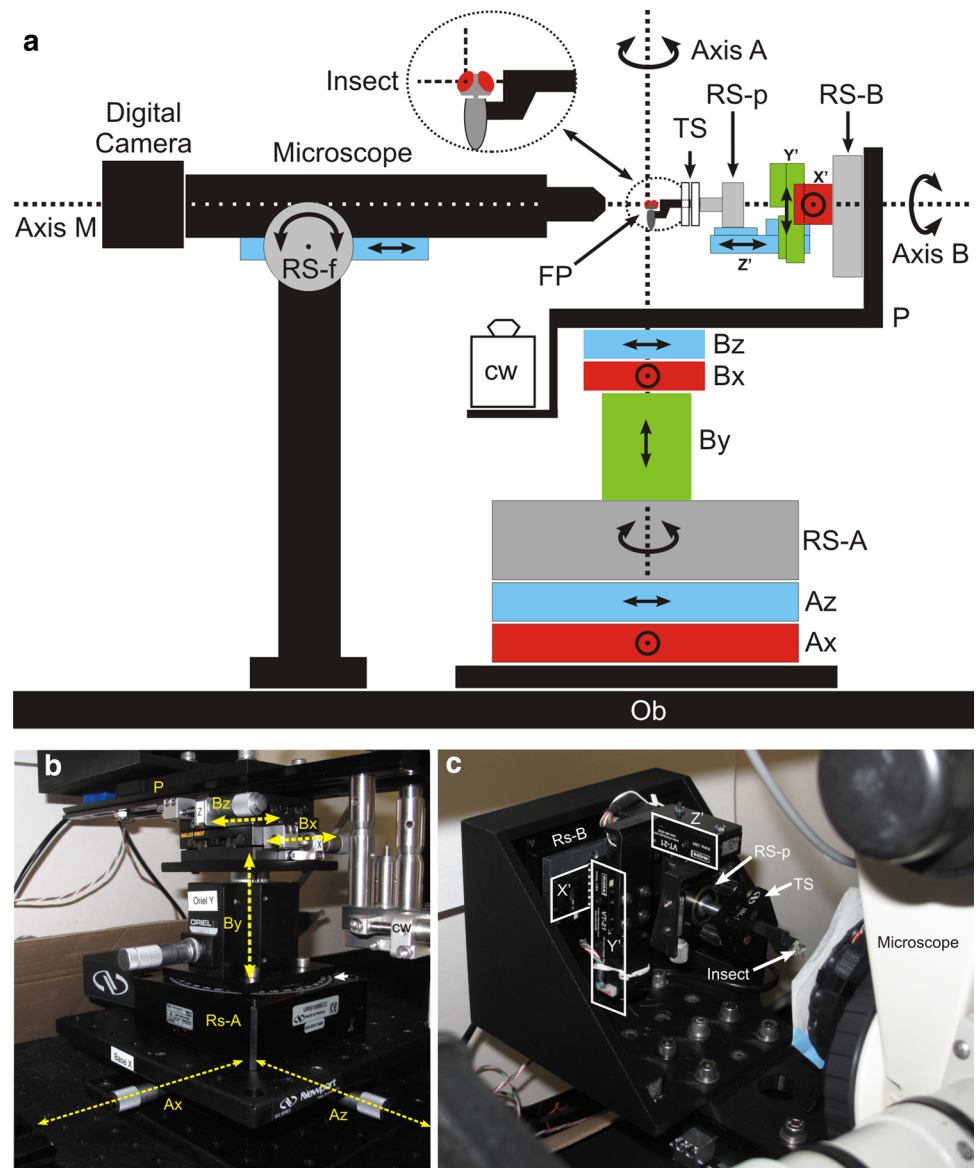


Fig. 1 Schematic diagram of the major electrical connections in the FACETS instrument. The PC (box at left) is used to control all electrical components except for those associated with microscope illumination (lower right). Dark gray shading denotes motor controllers; light gray, motorized stages. Components of the goniometer itself (at

right) are enclosed in a dashed rectangle: two rotary stages (RS-A and RS-B) and three linear translation stages (x' , y' , and z'). See text for additional details. *kbd* PC keyboard. *Nvidia* and *AMD*, graphics cards for the three PC monitors, *m1*, *m2*, and *m3*. *PCIE*, interface card for the camera

Fig. 2 Schematic and photographic views of the goniometer instrument. **a** Schematic goniometer elevation (at right) and microscope (upper left), drawn only approximately to scale. The insect (inset) and goniometer are shown at their initial orientations prior to sampling the eye, when the angular positions of rotary Axes *A* and *B* are at (0,0), and Axis *B* is parallel to the microscope's optical axis (Axis *M*). The eye's lateral surface faces the microscope, and its approximate center is positioned at the intersection of Axis *M* with the two rotary axes that orient the goniometer (Axis *A* and Axis *B*). The rotation and translation stages are color-coded, with gray for rotary axes (RS-), and red, green and blue for translation stages that move in the *x*, *y*, and *z* directions, respectively. The conventional 3-D Cartesian axes have been rotated so that the *z* axis is horizontal and corresponds to the optical axis of the microscope objective (see text). *FP* fixed point, *Ob* optical bench. **b**, **c** Photographs of the lower (b) and upper (c) portions of the goniometer. Counterweight (cw) is bolted to the platform (*P*) between upper and lower goniometer sections



rests on a vibration isolation table (Ealing model PM-26-1000, S. Natick, MA, USA).

The fixed point of the goniometer (Fig. 2a, FP) is defined as the intersection of the microscope's optical axis (Axis *M*) with the goniometer's two rotary axes (vertical Axis *A* and horizontal Axis *B*). Prior to making measurements, the angular positions of Axes *A* and *B* are set to (0,0), bringing Axis *B* parallel to Axis *M* as in Fig. 2a. The insect is mounted with the head facing upward, the lateral surface of one eye facing the microscope, and its position is adjusted so that the approximate center of that eye coincides with the fixed point. This specific orientation of the eye is important, because it aligns the goniometer's angular sampling range with the range of ommatidial angles that typically occur in insect eyes (see below).

In Fig. 2a, the four rotary stages are colored gray, and the translation stages are color-coded according to the initial orientations of their axes. The goniometer is composed of lower and upper portions that are separated by a platform (*P*) which supports the upper section. Motorized rotary stages RS-A and RS-B are used to view the specimen at different orientations. For example, by rotating Axis *A* between 0° and 90° and Axis *B* between -180° and +180°, a hemispherical range of eye orientations can be sampled. By further rotating Axis *A* to its upper limit of ~105° (beyond which the goniometer may collide with the microscope at some orientations), ~62 % of a complete spherical range can be sampled. This range is sufficient for completely characterizing the visual fields of many insect eyes, including frontal and posterior binocular zones,

without needing to remount the specimen. If the eyes have unusually extensive binocular overlap, complete sampling of the frontal field of view can be achieved by tilting the initial orientation of the head toward the microscope (counterclockwise in Fig. 2a), at the expense of omitting some posterior-viewing facets.

The performance characteristics of the motorized rotary stages are well suited for precise focusing and mapping of eye parameters. The microscope focusing is accurate to within $\sim 0.1 \mu\text{m}$, and the angular resolutions of the goniometer's two rotary stages are $\leq 0.001^\circ$, well below the smallest reported interommatidial angles in insects (0.1° – 0.3° ; Sherk, 1978b). The linear resolution of translation stages x' , y' , and z' is rated at 1 nm, and virtually no backlash is discernible when using microscope objective magnifications of at least $40\times$.

The five lower translation stages are used to align the goniometer, as explained in the “Appendix.” The remaining stages are used as follows. Motorized rotary stage RS-F focuses the image via a custom-built coupling to one of the microscope's focusing knobs. In the upper goniometer, the three motorized linear stages x' , y' , and z' are used to recenter the eye within the image plane independently of the angular orientation of the goniometer. These three stages are named according to their directions of movement when the goniometer is at its initial (0,0) orientation. A miniature rotation stage (RS-p, Newport #MT-RS) is used to adjust the initial pitch angle of the insect's head, and the roll and yaw angles are adjusted with a tilt stage (TS, Newport #MM-1).

Design features to minimize unwanted displacements

An ideal goniometer would rotate the specimen about a single point in space. In practice, all goniometers exhibit a finite “error volume” (Noiré et al. 2011) that arises from imprecision in the alignment of the rotary axes, imperfections in linear or rotary movements, and orientation-dependent bending or other displacements due to gravity-induced torques. In the current instrument, the precision of rotary axis alignment is mainly determined by the ca. 5 – $10 \mu\text{m}$ resolution of translation stages A_x , A_z , B_x , B_y and B_z (Fig. 2). To reduce other sources of error, the goniometer's overall orientation has been chosen to minimize changes in gravity-induced torques on those components which bear the heaviest loads. Thus, the axis of the primary rotary stage (Axis A) is oriented vertically to ensure relatively constant torques on all three rotary stages, as well as on the lower group of linear stages. In addition, cantilever forces are minimized with a counterweight (Fig. 2, cw) that shifts the upper components' center of mass close to Axis A. Measurements obtained by observing a 1-mm spherical ball bearing mounted in the goniometer showed that the

error volume was contained within a sphere with a radius of $\sim 75 \mu\text{m}$.

The goniometer's coordinate systems

The tabletop defines a fixed set of Cartesian axes with respect to gravity and the microscope. The microscope is oriented perpendicular to Axis A (thus horizontally), as this relationship is necessary to obtain a full range of subject views when the goniometer is rotated. Since a microscope's optical axis is conventionally defined as the “z” axis, whereas horizontal and vertical directions in the imaging plane are called “x” and “y,” the fixed Cartesian axes in Fig. 2 are labeled accordingly.

The motorized (x' , y' , and z') stages define a second set of Cartesian axes. The insect's head and eye define a third set of (x , y , and z) axes, and eye orientations are defined according to spherical coordinates of azimuth and elevation (Θ , Φ). Once the initial orientation of the head has been adjusted, the eye-centric orientations are fixed in relation to the x' , y' , and z' coordinate system, but they have been rotated, such that dorsoventral, anteroposterior, and left-to-right axes correspond to x' , y' , and z' . The software uses transformation matrices based on Euler angles (Goldstein et al. 2001) to relate the goniometer's angular coordinates to eye-centric spherical angular coordinates. For recentering the subject, an additional transformation matrix is used to compute how far the x' , y' , and z' stages should be moved to effect a net translation within the image plane (the microscope's focal plane), regardless of the current goniometer orientation.

Software control of the goniometer

The software to operate the instrument uses the Matlab Instrument Control, Image Acquisition and Image Analysis toolboxes. Graphical user interfaces assist the user in initializing the camera and motor controllers, aligning the camera, rotary axes, and insect eye, and generating a uniform spherical distribution of angular sampling orientations according to user-selection of the desired inter-sample angle (sampling density). The angular sampling distribution itself is computed using Distmesh, a public domain program for generating surface meshes (Persson and Strang 2004), and an efficient sampling path is pre-computed that begins at a virtual “pole” on the lateral surface of the eye (axes $A, B = 0, 0$) and proceeds along an expanding series of concentric latitudes.

Each time the goniometer rotates to a new sampling orientation, a series of automated steps is performed to refocus and recenter the eye (the automated focusing is described in the “Appendix”). A digital image is then saved to the hard disk, and morphological image processing steps

are used to measure features of the eye surface. The view of the specimen is refocused by adjusting the position of the microscope, and the specimen is recentered within the focal (x, y) plane by adjusting the motorized x' , y' , and z' stages.

The purpose of the recentering is to ensure that distance and area measurements from the surface of the eye are obtained where its curved surface is most nearly normal to the microscope's optical axis. This prevents measurement errors that could otherwise arise from viewing a tilted surface. The recentering algorithm is designed to identify the part of the eye that is normal to the microscope axis, while avoiding moving to a location beyond the edges of the eye. After recentering, the facet that lies closest to the center of the image is identified, a final recentering adjustment is made to position the centroid of this facet at the center of the image, and a final refocusing adjustment is performed before acquiring a final digital image that will be used for further processing. The processing of this final image consists of three basic stages: initial image-enhancing and contrast-standardizing steps, morphological image-processing steps to isolate individual facets as image "regions," and analyses to obtain the (x, y) coordinates of facet centers and measure the sizes of facets. Additional details of the auto-centering and image processing algorithms are described in the "Appendix."

Example eye measurements

The automated goniometer was used to obtain example facet diameter measurements from the eyes of four dipteran insects that have not previously been included in mapping studies, and they were selected because they exhibit substantial differences in the extent of an EFZ. A male *Phaenicia* sp. (Calliphoridae), a female soldier fly, *Odontomyia cincta* (Stratiomyidae), and a robber fly, *Efferia* sp. (Asilidae) were collected in northwest Florida (Okaloosa, Gulf and Walton Counties, respectively), and the small robber fly *Holcocephala fusca* (Asilidae) was collected in southern Maryland. Specimens were identified in general according to taxonomic keys (James 1981; Wood 1981; Shewell 1987). At the species level, *H. fusca* was identified by P. Gonzalez-Bellida, and *O. cincta* by comparing with specimens at the Florida State Arthropod collection (Gainesville, FL, USA) and the Archbold Biological Station (Venus, FL, USA).

Prior to initiating the sampling sequence, low-magnification views of the head at three orthogonal goniometer orientations were used to adjust the initial orientation in a highly repeatable manner. Frontal and dorsal views of the head and left–right symmetries were used to set both roll and yaw angles at 0° , and the initial pitch angle was set in relation to clearly identifiable landmarks on the head.

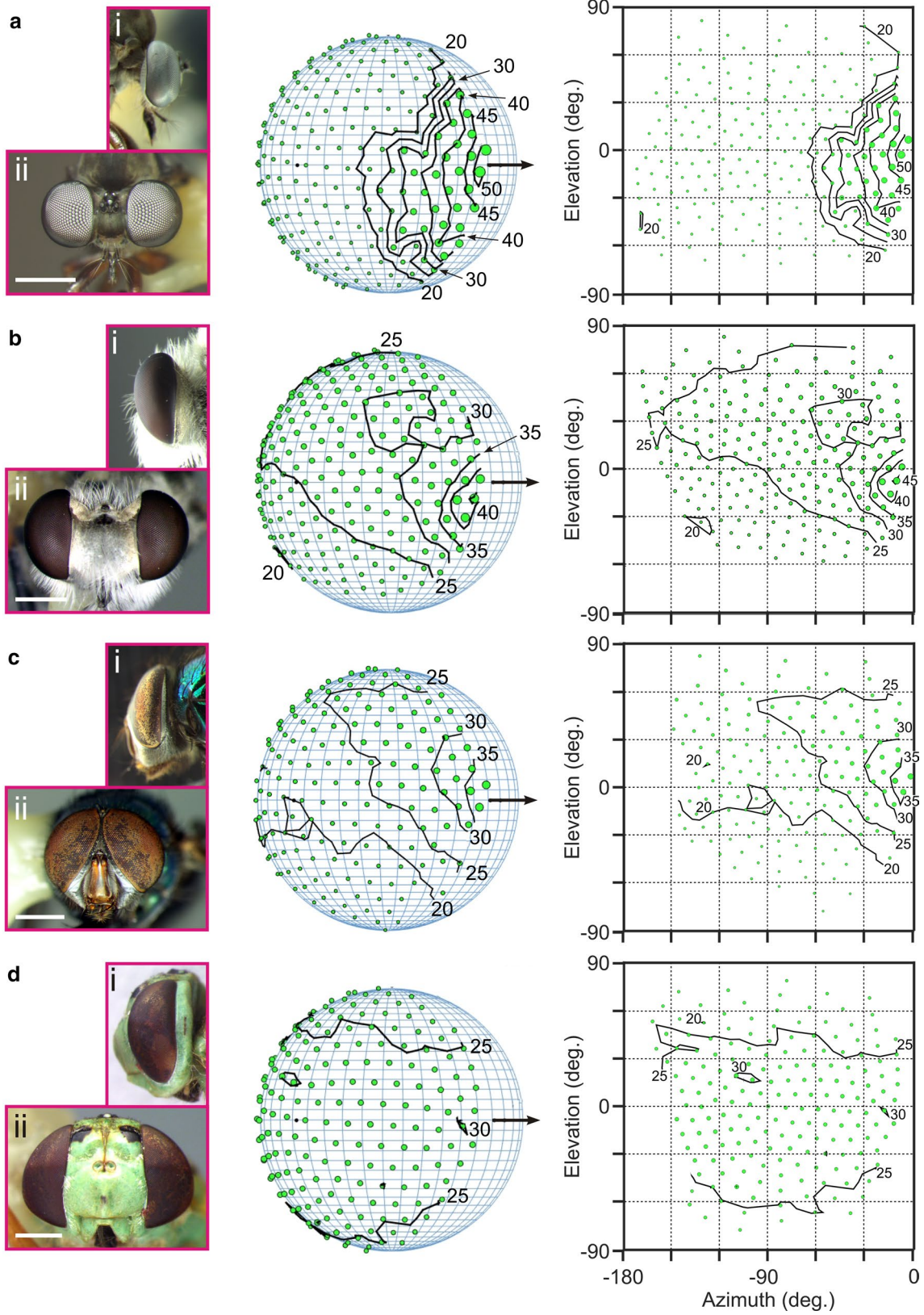
Fig. 3 Facet diameter maps measured from four dipteran species using the FACETS instrument. (**a** *Holcocephala fusca*, **b** male *Efferia* sp., **c** male *Phaenicia* sp., **d** female *Odontomyia cincta*). For each species, lateral (*i*) and frontal (*ii*) views of the heads of the specimens accompany the spherical and Mercator projections of facet diameter data in microns. In the plots, facet diameter contour lines are plotted at 5- μm intervals, and the diameters of the data points are scaled to be proportional to facet diameter. Each eye was examined using a uniform angular sampling distribution (**a** $N = 211$ orientations, **b** 216, **c** 165, **d** 180). To facilitate comparisons, all data are plotted as if they had been obtained from *right* eyes [the actual eyes that were measured are shown in the lateral eye views (*i*)]. The spherical plots have been rotated by 40° from lateral to emphasize the front of the eye. Dorsal is upward, and the anterior direction (0° in the Mercator projections) is indicated by horizontal arrows in the spherical plots. Scale bars **a–d** 1000 μm

Spherical and Mercator projections of the facet diameter data were plotted in Matlab, and then formatted in CorelDraw v.13 (Corel, Ottawa, Ontario). Diagrams and other figures were composed using CorelDraw 13 and Corel Photopaint v. 13. Contour lines were interpolated from the Mercator projections by using a function that is designed to handle data that are not distributed on a rectilinear grid (Hanselman 2012); those contours were then transformed to spherical coordinates for plotting on spherical projections.

Results

Measurements of facet diameters were made from four species of flies: two predatory robber flies (*Holcocephala fusca* and *Efferia* sp., Asilidae), and two non-predators—a male *Phaenicia* sp. (Calliphoridae) and a female *Odontomyia cincta* (Stratiomyidae). The body of *Holcocephala* is very small, but the eye is extremely large relative to its body size (Fig. 3a). The eyes and bodies of the other three species are roughly similar in size (Fig. 3b–d). To map the distributions of facet sizes, the goniometer was rotated sequentially to a uniformly distributed series of angular orientations. At each orientation, the specimen's position in the fixed (x, y) plane was then adjusted slightly to center the portion of the local eye surface that was normal to the optical axis of the microscope (see "Materials and methods").

One of the main aims of developing the FACETS instrument has been to demonstrate the feasibility of acquiring eye parameter data rapidly through automation. For eye mapping studies, a good measure of data acquisition speed is the sampling time per eye orientation, which is the time required to focus the goniometer, center the view, acquire and analyze images, and rotate the goniometer to the next sampling orientation. For the four data sets shown in Fig. 3, the mean time per orientation ranged from ca. 85 to 150 s. Since differences in the total numbers of sampled



orientations were relatively small and similar angular sampling densities were employed, the variability in sampling times may be mainly attributable to having studied the specimens at different times while the instrument's software was under development. The total time required to obtain measurements from a whole eye ranged from ~5 to 7 h, plus ~1 to 2 h of initial preparation time for mounting the specimen, adjusting goniometer alignment, setting the initial orientation of the head, and mapping the eye edges.

The plots in Fig. 3 show the distributions of the measured facet sizes as a function of eye azimuth and elevation. Zero and 180° of azimuth correspond to anterior and posterior directions, respectively, and vertical elevations range from -90° (ventral) to +90° (dorsal). To help visualize the 3-D angular orientations that were sampled, the data are plotted on both spherical and Mercator projections. Adjacent sampled orientations are separated by ~9°. Facet diameters are illustrated in two ways: the plotted diameters of individual data points are proportional to facet diameter, and contour lines are drawn at 5- μm intervals from 20 to 50 μm .

Among the four species examined, the total range of facet diameters was from ca. 15 to 54 μm . In the eyes of the asilid predators (*Holcocephala* and *Efferia*, Fig. 3a, b) and the male calliphorid fly (*Phaenicia*, Fig. 3c), there is a distinctive frontal EFZ in which the largest facets occur along the mediofrontal edge of the eye (Fig. 3a–c). Facet sizes in the posterior portions of these three eyes are much more uniform, particularly in *Holcocephala*, as evidenced by the nearly complete absence of contour lines at azimuth values <-60°. In contrast, the soldier fly *Odontomyia* (Fig. 3d) shows no evidence of a specialized frontal zone, and little regional variation in facet sizes, except that relatively small facets occur at orientations near the dorsal and ventral margins of the eye. In the majority of the *Odontomyia* eye (representing ~75 % of its total angular extent), facet diameters are nearly uniform, varying only from 25 to 30 μm .

Holcocephala has much smaller eyes than the other three species (see Fig. 3a photos), and shows the largest facet size gradient across an angular region that is smaller than corresponding areas in the eyes of either *Efferia* or *Phaenicia* (compare, for example, the 25- μm contours in Fig. 3a–c). Within *Holcocephala*'s zone of increasing facet sizes anterior to the 20 μm contour, facet diameters more than double, from 20 to 54 μm . In the rest of the eye, encompassing more than 75 % of its angular extent, the facets are small and remarkably uniform in size, ranging only between 16 and 20 μm . Despite its much smaller eyes, *Holcocephala* boasts the largest facets in this group (54 μm , compared to maximal diameters of 43 μm in *Efferia*, 40 μm in *Phaenicia*, and 31 μm in *Odontomyia*).

Because of species-specific differences among the eyes, the total solid angle that is represented by the sampled orientations varies somewhat. Expressed as percentages of a complete hemisphere (2π steradians), the sampled solid angles from *Holcocephala*, *Efferia*, *Phaenicia*, and *Odontomyia*, respectively, are ca. 86, 73, 69, and 74 %. Comparing the angular extents of the EFZs is not as straightforward, because of differences in the shapes and slopes of the individual zones. Nevertheless, by comparing regions where the same contour lines occur, it is clear that the angular extent of *Holcocephala*'s EFZ is the most compact overall, whereas those of *Efferia* and *Phaenicia* are more diffuse.

In the three species with an EFZ, it is also noteworthy that the overall topography of this zone is not radially symmetrical, and there are interspecific differences. In *Holcocephala*, beginning with the largest facets at the front of the eye, the EFZ appears to extend predominantly in a ventroposterior direction, roughly in a line extending from angular coordinates (0°,0°) to (-60°,-20°). In contrast, the EFZs of both *Efferia* and *Phaenicia* are biased dorsoposteriorly, in directions defined approximately by lines extending from (-5°,-10°) toward (-90°, +30°) in *Efferia*, and from (0°,0°) toward (-80°, +50°) in *Phaenicia*.

Discussion

Methods of mapping facet sizes

For purposes of mapping facet sizes, corneal replicas offer a potentially faster, simpler alternative to examining compound eyes at hundreds or thousands of precisely controlled orientations. Studies employing flattened corneal replicas have indeed provided useful comparative information about distributions of facet sizes across eye surfaces (e.g., Ribi et al. 1989; Narendra et al. 2011; Streinzer et al. 2013; Streinzer and Spaethe 2014). The resulting "maps," however, are limited, because they consist of 2-D projections that are unavoidably distorted and fragmented, and there appears to be no simple way to reconstruct them accurately into a quantitative 3-D framework. In contrast, facet sizes obtained by 3-D angular sampling methods are generally plotted on a spherical surface, preserving the three-dimensional character of the data. However, most compound eyes are not spherical, and both methods suffer from a lack (to the best of our knowledge) of any three-dimensional eye shape measurements. In the current investigation, since facet sizes sampled from a uniform angular distribution are presented on a sphere, relatively flat eye regions are under-represented, while more highly curved regions are over-represented. Probably the most significant consequence of this bias

applies to the asilid eyes, as their anterior-facing portions are quite noticeably flattened, and these areas correspond roughly to the EFZs. In terms of ocular surface area, this means that the two asilid EFZs occupy larger proportions of their respective eyes than suggested by the plots in Fig. 3a, b.

The potential significance of EFZs in predatory and male dipterans

Asilid flies are known as diurnally active visual predators that chase and capture other insects mainly in mid-flight (Lavigne and Holland 1969; Dennis and Lavigne 1975; LaPierre 2000; Marshall 2012). Although asilid eyes have long been known to have enlarged frontal facets (Walker 1851; Dietrich 1909), it appears that this feature has not previously been mapped in a quantitative manner. Dietrich's (1909) histological drawing of a vertical section through the eye of *Laphria flavia*, one of the larger members of the Asilidae, depicts greatly enlarged frontal ommatidia, with larger facets and considerably smaller interommatidial angles than in the dorsal and ventral ommatidia. This anatomical evidence is consistent with the presence of a frontal acute zone in *Laphria*, but direct measurements of acuity will be needed to confirm the extent to which EFZs in asilids truly correspond to acute zones.

The enlarged facets in *Holcocephala* and *Efferia* (Fig. 3a,b) clearly represent a specialization of the frontal visual field, and given the predatory lifestyle of asilids, the EFZs appear very likely to play a role in detecting and chasing prey. Similarly, as *Phaenicia* is related to non-predatory calliphorids and to muscid flies, and males in at least a few representatives of these families possess a high-acuity fronto-dorsal “love spot” (Beersma et al. 1977; Hardie 1979, 1986), the male *Phaenicia*'s frontal EFZ (Fig. 3c) may also be associated with a frontal acute zone that is used while chasing female conspecifics. As noted in the “Introduction,” zones with enlarged facets (EFZs) may be associated with acute zones, bright zones, or both.

Since *Holcocephala* and *Efferia* are both visually guided asilid predators, it would not be surprising if there were little difference between their EFZs. On the other hand, because they differ so much in body size, they almost certainly prey on distinct sets of prey species, and as a consequence, the details of their visual requirements while detecting or chasing prey may differ substantially. Indeed, the apparent differences in the shapes of their EFZs (Fig. 3a, b) suggest that they are the products of somewhat distinct selective pressures on visual performance. The presence of an elongated EFZ is reminiscent of distinctive dorsal and equatorial “foveal bands” of higher acuity that have been identified in different species of dragonfly eyes, and that

have also been suggested to reflect distinct visual requirements related to predation (Sherk 1978b).

Together, the data presented here support the expectation that much more can be learned about visual field specializations of compound eyes, by making more-detailed comparative investigations than have thus far been attempted. As was also mentioned in the “Introduction,” previous studies of both insects and crustaceans have mainly focused on the topography of acuity and its behavioral relevance in individual species, whereas comparative mapping studies are relatively rare. Particularly in view of the diversity of arthropods, the relationships between EFZs and AZs are nearly unknown.

Conclusions

The data examples presented here show that with higher levels of automation, broader comparative eye mapping studies are now quite feasible. The FACETS instrument also provides the basis for further refinements that will allow simultaneous evaluations of facet sizes and acuity (interommatidial angles). The resulting topographic maps will help reveal the extent to which these inter-related ommatidial specializations overlap or diverge (cf. van Hateren et al. 1989; Straw et al. 2006) in relation to behavioral differences. Studies of this kind are crucial not only for further understanding the sensory and ecological relevance of bright zones and acute zones, but more generally, the principles and constraints that govern the evolution of visual field specializations.

Acknowledgments The FACETS instrument was begun during a National Research Council (National Academies of Sciences) Senior Research Associateship to JKD at the Air Force Research Laboratory (AFRL), Eglin AFB, Florida, USA. Additional funding was provided by AFOSR LRIR grants 3003LW38 and 3003LW15. Funding for components of the goniometer instrument was provided by the AFRL Natural Systems Sensing Lab, and certain custom mounting adapters were produced at the Eglin Rapid Prototype Fabrication Facility. Several colleagues in Florida contributed helpful ideas and technical expertise during early development of the FACETS instrument, including Arunava Banerjee, Ben Dickinson, Eric Glatke, Dennis Goldstein, David Gray, Tony Thompson, and Jimmy Touma. *Holcocephala* specimens were provided by Paloma Gonzalez-Bellido. We wish to thank three anonymous reviewers for their critical comments, and especially Doekele Stavenga for suggestions on early versions of the manuscript.

Compliance with ethical standards

Animal studies This article does not contain any studies with animals performed by any of the authors.

Conflict of interest The authors declare that they have no conflict of interest.

Appendix

Microscope

The microscope is a Nikon metallurgical model, mounted on a boom stand and focused by adjusting its position, while the subject remains stationary. It is equipped with five long-working-distance Nikon M-Plan objectives (2.5×, 5×, 10×, 20× and 40×), an epi-illumination attachment, and a camera tube with 1.0× relay lens. The Grasshopper Express video camera is configured to provide 920 × 760 pixel 8-bit grayscale images, with a frame rate of ~15 Hz. Axial epi-illumination is provided by a 50-W tungsten halogen lamp, with an intervening heat filter (Newport FSR-KG3), field and aperture diaphragms, and removable neutral density, spectral and polarization filters.

Goniometer alignment

Prior to making measurements from the eye, rotary axes *A* and *B* are carefully aligned to the fixed point (Fig. 2a, FP) to minimize the amount of repositioning and refocusing that are required to keep the eye in view. Rotary axis alignment (Fig. 4) is accomplished by viewing each axis when it is parallel to the optical axis of the microscope objective (Fig. 4, Axis *M*), or is made to appear so with a mirror. Axis *A* is aligned first, because it cannot be moved without altering the position of Axis *B*. The rotary stage angles are positioned at (0,0), a vertical translation stage (Fig. 2a, By) is used to move the eye temporarily below Axis *M*, and a small rail-mounted first-surface mirror, precisely oriented at a 45° angle, is moved into place to provide an overhead view of the eye and render Axis *A* virtually parallel to Axis *M* (Fig. 4a). A landmark on the eye is chosen near the center of the field of view, and as Axis *A* is rotated, the circular trajectory of the landmark reveals the location of Axis *A* at the center of the circle. Specific translation stages (Ax and Az; Fig. 2a) are used to move Axis *A* toward the center, and other stages (Bx and Bz; Fig. 2a) are used to recenter the landmark.

After removing the mirror and bringing the side of the eye back into view (Fig. 4b), Axis *B* is aligned in the same way, now using stages Bx and By (Fig. 2a) to align Axis *B*, and stages *x'* and *y'* to recenter the eye. The accuracy of Axis *A* and *B* alignment is limited by the ca. 5 μm resolution of the micrometer adjustments on the corresponding translation stages (Ax and Az: Newport model 430; Bx and Bz: Melles Griot 2 × 2" stages; By: Oriel model 16611 vertical translation stage). The resolutions of motorized stages *x'*, *y'*, and *z'* are well under 5 μm, as previously noted in the main text.

Autofocusing

Autofocusing is accomplished by obtaining a series of images across a focusing range, evaluating the quality of focus of each image by computing a “focus index,” and then moving the microscope to the best focus level. Since higher-magnification objectives have shallower depths of field, a different focusing range is used for each objective. The microscope is first moved from its current position (usually, the level that was previously in focus before the eye was rotated) to one limit of the focusing range. As the microscope is scanned through the focusing range, a series of digital snapshots is obtained, and the focus index is computed from a circular region of interest (ROI) at the center of the image. The software increases the minimum ROI diameter of 100 pixels when the facet diameters currently in view exceed a certain threshold. The focus index is defined as the variance of the pixel brightness values within the ROI:

$$\text{Focus index} = \sum_{i=1 \text{ to } N} (I_i - I_m)^2 / N$$

where I_i is the intensity of the i th pixel, I_m is the mean pixel intensity, and N is the number of pixels in the ROI.

For a given scene that is viewed at several focus levels, the best-focused images tend to exhibit the highest variances, because local gradients in pixel brightness are steeper when edges and textures are in focus. The variance metric was chosen because previous tests of several

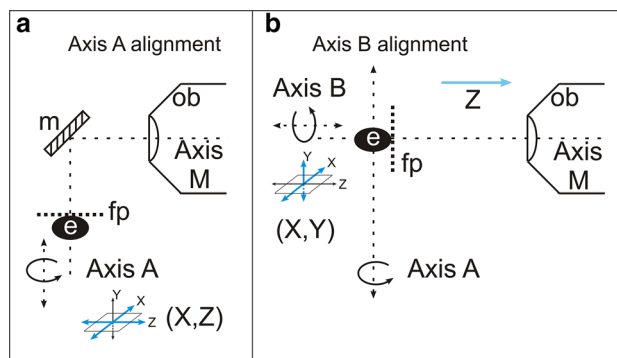


Fig. 4 Schematic overview of rotary Axis *A* and Axis *B* alignment procedures (see text for additional details). **a** To align axis *A*, the eye (*e*) is moved down below the objective axis (Axis *M*), and a 45° mirror (*m*) is moved into place to provide a view of the upper side of the eye. The position of Axis *A* in the (*x*,*z*) plane is determined by rotating the axis while viewing the eye, and using the appropriate translation stages to make Axis *A* coplanar with Axis *M*. **b** After removing the mirror, moving the eye up to bring the side of it back into view, and refocusing the microscope in the *Z* direction, the same procedure is used to adjust Axis *B* within the (*x*,*y*) plane until it coincides with Axis *M*. *fp* focal plane, *ob* microscope objective

alternative image-processing filters have shown this to be one of the most robust indicators of focusing quality (Sun et al. 2004), and preliminary tests of focusing on the surfaces of insect eyes demonstrated its effectiveness.

Each time the eye is rotated to a new orientation, focusing scans are used in two ways. First, a focusing scan is used to obtain information that will be used for recentering the eye. In this case (see “[Recentering](#),” below), the image obtained at each focus level is divided into a grid of rectangular ROIs, and a local focus index is calculated from each ROI. Second, after recentering the eye, a final focusing scan and focusing adjustment is performed before acquiring the image that will actually be used to represent the view at the current orientation. For this purpose, only the central portion of the current view is of interest, so a single ROI is used at the center of the image, and for symmetry, this ROI is defined to be circular instead of rectangular. After the final focusing adjustment, three “live” video snapshots are averaged to reduce random noise in the images, and the mean image is saved to a file and also used for additional image processing (see “[Image processing to measure ommatidial parameters](#),” below).

Recentering

After the eye has been rotated to a new orientation, its position within the vertical (“x,y”) focal plane is adjusted so as to center the portion of the eye that lies closest to the microscope objective. The purpose of this step is to ensure that distance and area measurements from the surface of the eye are made where its curved surface is most nearly normal to the microscope’s optical axis. This avoids measurement errors that could otherwise arise from viewing a tilted surface, and ensures that the eye surface is viewed in a consistent manner at each sampled orientation.

To identify the portion of the eye that lies closest to the microscope, the automated code first performs a focusing scan to bring the center of the current view into focus. Each image is divided into a grid of ROIs, and a focus index is calculated from each ROI. Next, the best-focused image level at each ROI location is used to construct a mosaic image in which each ROI is relatively well focused. Morphological image processing operations (see “[Image processing to measure ommatidial parameters](#),” below) are then applied to exclude certain portions of the mosaic image that do not appear consistent with certain characteristics of compound eyes, as these parts of the image may represent locations outside of the boundaries of the eye. (Since the faceted surfaces of compound eyes are highly structured, they generally exhibit many edges. Thus, any ROI with a paucity of edges at its best focus level is excluded from further analysis.) The remaining ROI regions are used to create a 3-D topographic surface plot of eye “elevations” in the Z direction, and the

eye is recentered, so as to position the maximum “elevation” at the center of the image. The final centering step is to identify the facet that is closest to the center of the image (see “[Image processing to measure ommatidial parameters](#),” below) and position it precisely at the center.

Image processing to measure ommatidial parameters

Various image processing functions (many of which are provided in the MATLAB image processing toolbox) are used to enhance raw images and extract information about the sizes and locations of identifiable structures. Only the main steps are described here. After an eye sampling and image processing session, a separate MATLAB program is used to review the automated image processing results and correct any errors.

Using an averaged image from at least three snapshots, the image contrast is standardized by normalizing the range of pixel intensities to the full 8-bit gray scale, and a Gaussian smoothing operation is applied to minimize small bright or dark artifacts (Fig. 5a). A morphological “image opening” operation is applied to this image to help isolate the facets, but this operation should be scaled to the approximate sizes of the facets themselves. Therefore first, the bright white highlights on the convex surfaces of facets are used to provide a preliminary estimate of inter-facet distances. Due to the curvature of the eye surface, highlights and facet centers do not always coincide, but their spacing is similar. The grayscale image in Fig. 5a is converted to a thresholded binary (black and white) image (Fig. 5b), isolating the highlights as white spots on a uniform black background. The inter-highlight distance is then defined as the mean distance from the centroid of the most centrally located spot to the centroids of its four nearest neighbors (see Fig. 5b, blue lines). Returning to the previous grayscale image (Fig. 5a), an image opening step scaled to the inter-highlight distance renders each facet as a convex, relatively bright region surrounded by darker borders (Fig. 5c), and a “watershed” operation identifies individual facets as separate image regions with contiguous borders (Fig. 5c, yellow outlines). Finally, the local facet diameter is defined as the mean distance between the centroids of the most centrally located region and its four nearest neighbors (Fig. 5d, blue lines). To help the user visualize the facet lattice and evaluate the results of each processed image, the FACETS software marks the nine most centrally located centroids (Fig. 5d, yellow dots), and a Voronoi diagram, which depicts facet edges based on the centroid coordinates, is superimposed (Fig. 5d, yellow lines).

Using the mean of four inter-centroid distances as a proxy for facet diameters helps minimize possible errors due to image artifacts (e.g., from small specks of debris), which can distort the estimated dimensions of single facet regions. The distance measure also serves reasonably well regardless of the local geometry of the facet lattice. In eye

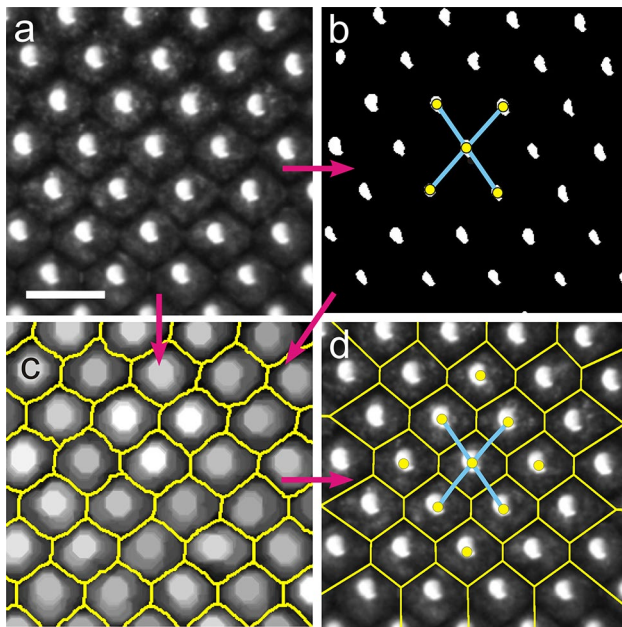


Fig. 5 Illustration of automated image processing steps that are used at each goniometer orientation to identify facets, locate facet centroid coordinates, and measure facet diameters. This view is from the anterior EFZ in *Efferia* (see Fig. 3b). **a** Grayscale image of the eye surface after averaging ($N = 3$), contrast enhancement and Gaussian smoothing. Regularly-spaced bright white spots are specular highlights reflected from the convex surfaces of cuticular corneas. **b** Binary (black and white) image from **a**, in which white spots correspond to the highlights. The mean inter-highlight distance is defined as the mean distance between the centroids of the most centrally located highlight and its four nearest neighbors (connected to the central highlight with blue lines). **c** Grayscale image from **a**, following an image “opening” step that has been scaled to the inter-highlight distance to emphasize facets, not highlights. Using the image in **c**, additional image processing steps identify individual facets (regions within yellow borders). **d** The final processing steps (here superimposed on the image from **a**) use the distances (blue lines) among the five most-central facet centroids (yellow dots) to measure the “local facet diameter” (see text for additional details). Arrows depict the overall flow of information during image processing. Scale bar in **a** = 50 μm

regions where the facet lattice is hexagonal, inter-centroid distances correspond to the diameters of the nearly circular facets. In areas where the geometry is more square than hexagonal, the nearest four distances correspond to facet widths. Only the four nearest centroids are used, because in more-square regions, the distances to the fifth- and sixth-closest centroids would overestimate the desired measurement by as much as $\sqrt{2}$.

References

- Beersma DGM, Stavenga DG, Kuiper JW (1975) Organization of visual axes in the compound eye of the fly *Musca domestica* L. and behavioural consequences. *J Comp Physiol* 103:305–320
- Beersma DGM, Stavenga DG, Kuiper JW (1977) Retinal lattice, visual field and binocularities in flies. Dependence on species and sex. *J Comp Physiol* 119:207–220
- Collett TS, Land MF (1975) Visual control of flight behavior in the hoverfly *Syrirta pipiens* L. *J Comp Physiol* 99:1–76
- Cronin TW, Johnsen S, Marshall NJ, Warrant EJ (2014) *Visual Ecology*. Princeton University Press, Princeton
- Dahmen H (1991) Eye specialisation in waterstriders: an adaptation to life in a flat world. *J Comp Physiol A* 169:623–632
- Dennis DS, Lavigne RJ (1975) Comparative behavior of Wyoming robber flies II (Diptera: Asilidae). Agricultural experiment station, University of Wyoming, no 30
- Dietrich W (1909) Die facettenaugen der Dipteren. *Z Wiss Zool* 92:465–539
- Franceschini N, Kirschfeld K (1971) Étude optique *in vivo* des éléments photorécepteurs dans l’oeil composé de *Drosophila*. *Kybernetik* 8:1–13
- Goldstein H, Poole C, Safco J (2001) *Classical mechanics*, 3rd edn. Addison Wesley, San Francisco
- Gonzalez-Bellido PT, Wardill TJ, Jausola M (2011) Compound eyes and retinal information processing in miniature dipteran species match their specific ecological demands. *PNAS* 108(10):4224–4229
- Hanselman D (2012) Tricontour function (BSD-licensed code downloaded from the Mathworks File Exchange. www.mathworks.com/matlabcentral/fileexchange. Accessed 22 Aug 2013)
- Hardie RC (1979) Electrophysiological analysis of the fly retina. I. Comparative properties of R1–6 and R7 and R8. *J Comp Physiol A* 129:19–33
- Hardie RC (1986) The photoreceptor array of the dipteran retina. *Trends Neurosci* 9:419–423
- Horridge GA (1978) The separation of visual axes in apposition compound eyes. *Phil Trans R Soc Lond B* 285:1–59
- Horridge GA, Duelli P (1979) Anatomy of the regional differences in the eye of the mantis *Ciulfina*. *J Exp Biol* 80:165–190
- James MT (1981) Stratiomyidae. In: McAlpine JF (ed) *Manual of nearctic diptera*, vol I. Biosystematics Research Institute, Ottawa, Ontario. Monogr 27, pp 497–511
- Krapp HG, Gabbiani F (2005) Spatial distribution of inputs and local receptive field properties of a wide-field, looming sensitive neuron. *J Neurophysiol* 93:2240–2253
- Land MF (1981) Optics and vision in invertebrates. In: Autrum H (ed) *Handbook of sensory physiology*, vol VII/6B. Springer, Berlin, pp 471–592
- Land MF (1989) Variations in the structure and design of compound eyes. In: Stavenga DG, Hardie RC (eds) *Facets of vision*. Springer, Berlin, pp 90–111
- Land MF (1997) Visual acuity in insects. *Ann Rev Entomol* 42:147–177
- Land MF (1999) Compound eye structure: matching eye to environment. In: Archer SN, Djamgoz MBA, Loew ER, Partridge JC, Vallerga S (eds) *Adaptive mechanisms in the ecology of vision*. Kluwer, Dordrecht, pp 51–71
- Land MF, Eckert H (1985) Maps of the acute zones of fly eyes. *J Comp Physiol A* 156:525–538
- Land MF, Nilsson D-E (2002) *Animal eyes*. Oxford University Press, Oxford
- LaPierre LM (2000) Prey selection and diurnal activity of *Holcocephala oculata* (F.) (Diptera: Asilidae) in Costa Rica. *Proc Entomol Soc Wash* 102:643–651
- Lavigne RJ, Holland FR (1969) Comparative behavior of eleven species of Wyoming robber flies (Diptera: Asilidae). Agricultural Experiment Station, University of Wyoming, Wyoming
- Marshall SA (2012) *Flies: the natural history and diversity of diptera*. Firefly Books, Buffalo

- Marshall J, Land MF (1993) Some optical features of the eyes of stomatopods. I. Eye shape, optical axes and resolution. *J Comp Physiol A* 173:565–582
- Narendra A, Reid SF, Greiner B, Peters RA, Hemmi JM, Ribi W, Zeil J (2011) Caste-specific visual adaptations to distinct daily activity schedules in Australian *Myrmecia* ants. *Proc R Soc Lond B* 278:1141–1149
- Noiré P, Jonquerès N, Schlutig S, Leterme D, Roux T (2011) Sphere of confusion of a goniometer: measurements, techniques and results. *Diam Light Sour Proc* 1(e28):1–4
- Persson P-O, Strang G (2004) A simple mesh generator in MATLAB. *SIAM Rev* 46(2):329–345
- Petrowitz R, Dahmen H, Egelhaaf M, Krapp HG (2000) Arrangement of optical axes and spatial resolution in the compound eye of the female blowfly *Calliphora*. *J Comp Physiol A* 186:737–746
- Ribi WA, Engels E, Engels W (1989) Sex and caste specific eye structures in stingless bees and honey bees (Hymenoptera: Trigoniidae, Apidae). *Entomol Generalis* 14:233–242
- Roberts NW, How MJ, Porter ML, Temple SE, Caldwell RL, Powell SB, Gruev V, Marshall NJ, Cronin TW (2014) Animal polarization imaging and implications for optical processing. *Proc IEEE* 102(10):1427–1434
- Rossel S (1979) Regional differences in photoreceptor performance in the eye of the praying mantis. *J Comp Physiol A* 131:95–112
- Rutowski RL, Gislén L, Warrant EJ (2009) Visual acuity and sensitivity increase allometrically with body size in butterflies. *Arthropod Struct Dev* 38(2):91–100
- Sherk TE (1977) Development of the compound eyes of dragonflies (Odonata). I. Larval compound eyes. *J Exp Zool* 201:391–416
- Sherk TE (1978a) Development of the compound eyes of dragonflies (Odonata). II. Development of the larval compound eyes. *J Exp Zool* 203:47–59
- Sherk TE (1978b) Development of the compound eyes of dragonflies (Odonata). III. Adult compound eyes. *J Exp Zool* 203:61–79
- Shewell GE (1987) Calliphoridae. In: McAlpine JF (ed) *Manual of nearctic diptera*, vol II. Biosystematics Research Institute, Ottawa, Ontario. Monogr 28, pp 1133–1145
- Smolka J, Hemmi JM (2009) Topography of vision and behavior. *J Exp Biol* 212:3522–3532
- Somanathan H, Kelber A, Borges RM, Wallén R, Warrant EJ (2009) Visual ecology of Indian carpenter bees II: adaptations of eyes and ocelli to nocturnal and diurnal lifestyles. *J Comp Physiol A* 195:571–583
- Stavenga DG (1979) Pseudopupils of compound eyes. In: Autrum H (ed) *Vision in invertebrates: handbook of sensory physiology*, vol VII/6A. Springer, Berlin, pp 357–439
- Stavenga DG (1992) Eye regionalization and spectral tuning of retinal pigments in insects. *Trends Neurosci* 15:213–218
- Straw AD, Warrant EJ, O'Carroll DC (2006) A 'bright zone' in male hoverfly (*Eristalis tenax*) eyes and associated faster motion detection and increased contrast sensitivity. *J Exp Biol* 209:4339–4354
- Streinzer M, Spaethe J (2014) Functional morphology of the visual system and mating strategies in bumblebees (Hymenoptera, Apidae, *Bombus*). *Zool J Linn Soc* 170:735–747
- Streinzer M, Brockmann A, Nagaraja N, Spaethe J (2013) Sex and caste-specific variation in compound eye morphology of five honeybee species. *PLoS One* 8:e57702
- Sun Y, Duthaler S, Nelson BJ (2004) Autofocusing in computer microscopy: selecting the optimal focus algorithm. *Microsc Res Tech* 65:139–149
- van Hateren JH, Hardie RC, Rudolph A, Laughlin SB, Stavenga DG (1989) The bright zone, a specialized dorsal region in the male blowfly *Chrysomya megalocephala*. *J Comp Physiol A* 164:297–308
- Walker F (1851) *Insecta Britannica*, vol 1. London. Cited by Melin D (1923). Contributions to the knowledge of the biology, metamorphosis and distribution of the Swedish asilids. *Zool Bidrag Uppsala* 8:1–318
- Warrant E, Kelber A, Frederiksen R (2007) Ommatidial adaptations for spatial, spectral, and polarization vision in arthropods. In: North G and Greenspan RJ (eds) *Invertebrate neurobiology*. Cold Spring Harbor Laboratory Press, Cold Spring Harbor, New York. Monograph 49, pp 123–154
- Warrant E, Oskarsson M, Kalm H (2014) The remarkable visual abilities of nocturnal insects: neural principles and bioinspired night-vision algorithms. *Proc IEEE* 102(10):1411–1426
- Wood GC (1981) Asilidae. In: McAlpine JF (ed) *Manual of nearctic diptera*, vol I. Biosystematics Research Institute, Ottawa, Ontario. 27: 549–574
- Zeil J, Nalbach G, Nalbach H-O (1986) Eyes, eye stalks and the visual world of semi-terrestrial crabs. *J Comp Physiol A* 159(6):801–811